12. J. M. Fierro, P. F. Michelson, P. L. Nolan, D. J. Thompson, *Astrophys. J.* **494**, 734 (1998).
13. A. Abdo *et al.*, *Astrophys. J.* **708**, 1254 (2010).
14. R. N. Manchester, G. B. Hobbs, A. Teoh, M. Hobbs, *Astron. J.* **129**, 1993 (2005).
15. ATNF Pulsar Catalogue, www.atnf.csiro.au/people/pulsar/psrcat/.
16. T. C. Weekes *et al.*, *Astrophys. J.* **342**, 379 (1989).
17. E. Aliu *et al.*; MAGIC Collaboration, *Science* **322**, 1221 (2008).
18. J. Albert *et al.*, *Astrophys. J.* **674**, 1037 (2008).
19. J. Holder *et al.*, *Astropart. Phys.* **25**, 391 (2006).
20. A. M. Hillas, in Proceedings of the 19th International Cosmic Ray Conference, La Jolla, CA, 11 to 23 August 1985, p. 445 (ICRC, La Jolla, 1985).
21. P. Cogan, in Proceedings of the 30th International Cosmic Ray Conference, Mérida, Mexico, 3 to 7 July 2007, vol. 3, p. 1385 (ICRC, Mérida, 2008).
22. A. G. Lyne *et al.*, *Mon. Not. R. Astron. Soc.* **265**, 1003 (1993).
23. Jodrell Bank Crab Pulsar Monthly Ephemeris, www.jb.man.ac.uk/~pulsar/crab.html.
24. O. C. de Jager, *Astrophys. J.* **436**, 239 (1994).
25. X.-N. Bai, A. Spitkovsky, *Astrophys. J.* **715**, 1282 (2010).
26. M. G. Baring, *Adv. Space Res.* **33**, 552 (2004).
27. K. J. Lee *et al.*, *Mon. Notic. Roy. Astron. Soc.* **405**, 2103 (2010).
28. M. Lyutikov, A. N. Otte, A. McCann, arXiv:1108.3824 (2011).
29. R. W. Lessard *et al.*, *Astrophys. J.* **531**, 942 (2000).
30. The Fermi-LAT pulse profile of the Crab pulsar above 100 MeV that is shown in Fig. 1 is not the original one from reference (*13*) but one that has been calculated with an updated ephemerides that corrects for a small phase offset that has been introduced in the original analysis http://fermi.gsfc.nasa.gov/ssc/data/access/lat/ephems/0534+2200/README.
31. M. de Naurois *et al.*, *Astrophys. J.* **566**, 343 (2002).
32. F. Aharonian *et al.*, *Astrophys. J.* **614**, 897 (2004).
33. S. Oser *et al.*, *Astrophys. J.* **547**, 949 (2001).

Dispersible Exfoliated Zeolite Nanosheets and Their Application as a Selective Membrane

Kumar Varoon,* Xueyi Zhang,* Bahman Elyassi, Damien D. Brewer, Melissa Gettel,†
Sandeep Kumar,‡ J. Alex Lee,§ Sudeep Maheshwari,‖ Anudha Mittal, Chun-Yi Sung,
Matteo Cococcioni, Lorraine F. Francis, Alon V. McCormick, K. Andre Mkhoyan, Michael Tsapatsis¶

Thin zeolite films are attractive for a wide range of applications, including molecular sieve membranes, catalytic membrane reactors, permeation barriers, and low-dielectric-constant materials. Synthesis of thin zeolite films using high-aspect-ratio zeolite nanosheets is desirable because of the packing and processing advantages of the nanosheets over isotropic zeolite nanoparticles. Attempts to obtain a dispersed suspension of zeolite nanosheets via exfoliation of their lamellar precursors have been hampered because of their structure deterioration and morphological damage (fragmentation, curling, and aggregation). We demonstrated the synthesis and structure determination of highly crystalline nanosheets of zeolite frameworks MWW and MFI. The purity and morphological integrity of these nanosheets allow them to pack well on porous supports, facilitating the fabrication of molecular sieve membranes.

High-aspect-ratio zeolite single crystals with thickness in the nanometer range (zeolite nanosheets) are desirable for applications including building blocks for heterogeneous catalysts (*1–3*) and the fabrication of thin molecular sieve films and nanocomposites for energy-efficient separations (*4*). They could also be of fundamental importance in probing the mechanical, electronic, transport, and catalytic properties of microporous networks at the nanoscale (*5*, *6*). Despite steady advances in the preparation and characterization of layered materials containing microporous layers and of their pillared and swollen analogs (*1–3*, *7–17*), the synthesis of suspensions containing discrete, intact, nonaggregated zeolite nanosheets has proven elusive because of structural deterioration and/or aggregation (*18*) of the lamellae upon exfoliation. Here, we report the isolation and structure determination of highly crystalline zeolite nanosheets of the MWW and MFI structure types, and we demonstrated the use of their suspensions in the fabrication of zeolite membranes.

MWW and MFI nanosheets were prepared starting from their corresponding layered precursors ITQ-1 (*1*) and multilamellar silicalite-1 (*3*), respectively. Before exfoliation by melt blending with polystyrene (weight-average molecular weight = 45000 g/mol), ITQ-1 was swollen according to a previously reported procedure (*18*); multilamellar silicalite-1 was used as made. Melt blending was performed under a nitrogen environment in a co-rotating twin screw extruder with a recirculation channel (*19*). The polystyrene nanocomposites obtained by melt blending were characterized by x-ray diffraction (XRD), and microtomed sections were imaged by transmission electron microscopy (TEM) to reveal the presence of exfoliated MWW and MFI nanosheets embedded in the polymer matrix (figs. S1 and S2).

To obtain a dispersion of these nanosheets, the nanosheet-polystyrene nanocomposites were placed in toluene and sonicated. After polymer dissolution and removal of the larger particles by centrifugation, the dispersions, containing approximately 1.25% w/w polymer and 0.01% w/w nanosheets, were used to prepare samples for TEM and atomic force microscopy (AFM) examination, by drying a droplet on TEM grids and freshly cleaved mica surfaces, respectively (the AFM sample was calcined in air at 540°C to remove polymer). Low-magnification TEM images of high-aspect-ratio MWW and MFI nanosheets reveal their flakelike morphology (Fig. 1, A and B). The uniform contrast from isolated nanosheets suggests uniform thickness, whereas the darker areas can be attributed to overlapping of neighboring nanosheets. Although lattice fringes are not easily visible in the high-resolution TEM (HRTEM) images of the nanosheets (figs. S3A and B), they do exist, as confirmed by their fast Fourier transform (FFT) (figs. S3C and D). In addition, electron diffraction (ED) from single MWW and MFI nanosheets (Fig. 1, C to E, and G) and XRD data obtained from calcined powders of MWW and MFI nanosheets (Fig. 2, A and B) confirm that the nanosheets are highly crystalline materials of the MWW and MFI type, respectively. The thin dimensions of MWW and MFI nanosheets, as expected, are along the *c* and *b* axes, respectively, as indicated from the FFT of the HRTEM images and the ED data.

AFM measurements, calibrated using steps formed on freshly cleaved mica (*20*), revealed

Department of Chemical Engineering and Materials Science, University of Minnesota, 151 Amundson Hall, 421 Washington Avenue Southeast, Minneapolis, MN 55455, USA.

*These authors contributed equally to this work.
†Present address: Department of Chemical and Environmental Engineering, University of California, Riverside, 1175 West Blaine Street, Riverside, CA 92507, USA.
‡Present address: Material Analysis Laboratory, Intel Corporation, Hillsboro, OR 97124, USA.
§Present address: Department of Chemical and Biomolecular Engineering, Rice University, MS-362, 6100 Main Street, Houston, TX 77005, USA.
‖Present address: Schlumberger Doll-Research, Schlumberger Limited, 1 Hampshire Street, Cambridge, MA 02139, USA.
¶To whom correspondence should be addressed. E-mail: tsapatsis@umn.edu

Fig. 1. Low-magnification TEM images of *c*-oriented MWW (**A**) and *b*-oriented MFI nanosheets (**B**). TEM images of single MWW and MFI nanosheets are shown in (**C**) and (**D**), respectively. (**E**) and (**G**) are the corresponding ED patterns of the same particles shown in (C) and (D), respectively. Simulations of the ED patterns of proposed structures of nanosheets down the *c* axis (MWW) and *b* axis (MFI) are shown in (**F**) and (**H**), respectively. Scale bars in (A) to (C), 200 nm; in (D), 50 nm; in (E) and (G), 1 nm^{-1}.
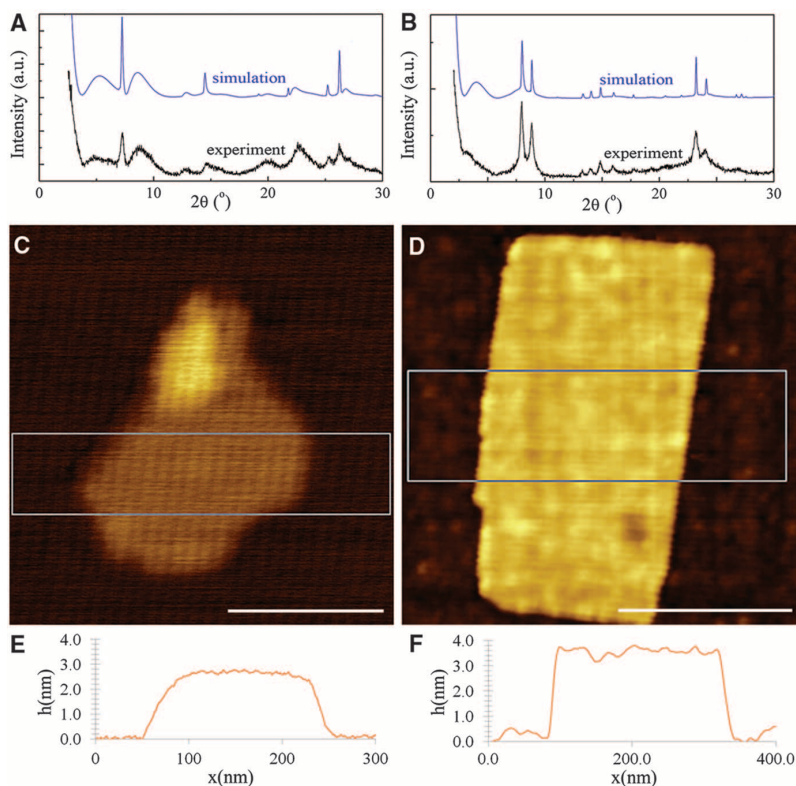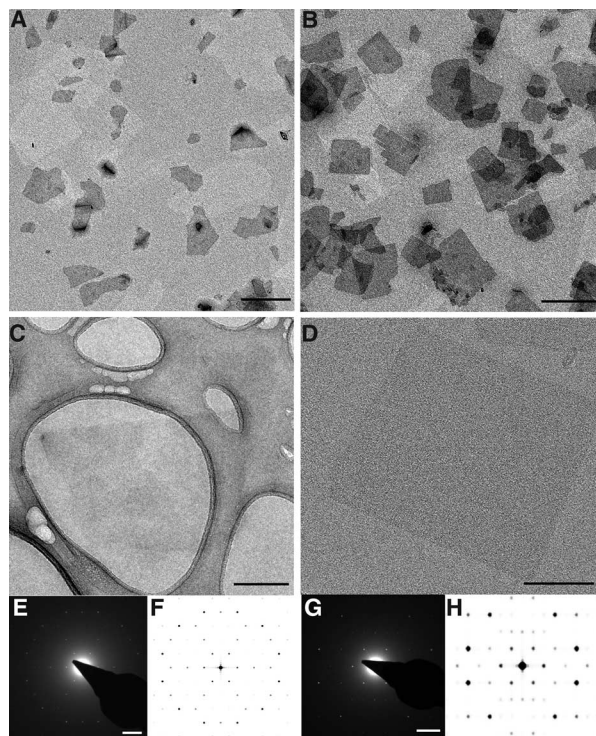

Fig. 2. Powder XRD pattern from MWW nanosheets (**A**) and MFI nanosheets (**B**). a.u., arbitrary units. The bottom traces show experimental XRD patterns (Cu Kα source, wavelength = 1.5418 Å) of the powder obtained by calcination of the nanosheet-polystyrene nanocomposite at 540°C. The top traces are the simulated XRD patterns (powder pattern theorem, implemented with UDSKIP) of the proposed structure of the nanosheets. AFM (tapping mode) topographical images of MWW and MFI nanosheets are shown in (**C**) and (**D**), respectively. The average step-height (h) data of the area highlighted in (C) and (D) are plotted in (**E**) (MWW nanosheet) and (**F**) (MFI nanosheet). The height data are calibrated using steps formed on freshly cleaved mica. Scale bars in (C) and (D), 200 nm.

remarkable uniformity in nanosheet thickness: 2.6 ± 0.3 and 3.4 ± 0.3 nm for the MWW and MFI nanosheets, respectively (Fig. 2, C to E, and F). The MWW nanosheet thickness is close to the one expected from the thickness of the ITQ-1 layers (2). Figure 3, A and B, show side and top views of the proposed MWW nanosheet structure that are consistent with the AFM measurements and MWW layer structure. The MFI nanosheet thickness, determined by AFM, is consistent with 1.5 unit cells along the *b* axis. Further examination of the HRTEM images collected here (fig. S4) and of the images given in (3), in conjunction with the thickness determined by AFM, suggests the presence of three complete pentasil chains running along the nanosheets. The proposed structure of MFI nanosheets based on these data is shown in Fig. 3C (side view along *c* axis) and Fig. 3D (top view). A $Q^3/(Q^3 + Q^4)$ ratio of 11% is calculated from this model, which is in agreement with the ^{29}Si magic angle spinning nuclear magnetic resonance data (fig. S5).

The proposed structures of the MWW and MFI nanosheets are consistent with all the TEM, ED, and AFM data and the structures of their precursors (Fig. 3). Optimization of nanosheet structures using damped-dynamics simulation by the Car-Parrinello molecular dynamics code in the Quantum ESPRESSO package (21) [see details in the supporting online material (SOM) (22)] led to minor changes (fig. S6) when compared to those obtained by simple termination of the MWW and MFI structures. More specifically, the calculated MWW and MFI nanosheet thicknesses are slightly different as compared to the ones obtained from the MWW and MFI frameworks (2.63 nm versus 2.49 nm and 3.20 nm versus 3.21 nm, respectively), and both are in agreement with the AFM measurements. The corresponding ED and XRD patterns from the optimized structures were simulated [see details in (22)] and compared to the experimental data. The ED pattern simulations (Fig. 1, F and H), performed with the Multislice method (23, 24), are in agreement with the experimental ED patterns (Fig. 1, E and G). Moreover, XRD simulations [using the powder pattern theorem, implemented with the UDSKIP algorithm (25, 26)] are also in good agreement with the experimental XRD data (Fig. 2, A and B). The positions of the broad peaks at low angles are very sensitive to the layer thickness and confirm the thickness suggested by AFM. More specifically, simulations using MFI nanosheet thicknesses of 1, 1.5, 2.5, and 3.5 unit cells (fig. S7) showed that the best agreement with the experimental data is obtained for the 1.5-unit-cell thickness, whereas the MWW simulations indicated 1-unit-cell thickness. The position of the sharper peaks at higher angles is insensitive to the layer thickness. They indicate long-range order preservation upon exfoliation. The XRD analysis of MFI nanosheets shows sharper reflections as compared to those of MWW nanosheets, probably due to the differences in thicknesses and the

better structural preservation of MFI nanosheets. The latter could be attributed to the absence of the swelling step in their processing.

Previous attempts to obtain exfoliated nanosheets of MWW have had only partial success because of the fragmentation, aggregation, and curling of the lamellae (*13, 19, 27*), whereas exfoliation of lamellar silicalite-1 has not been reported before. Our attempts to remove the polystyrene by methods that include calcination or other thermal treatments of the nanosheet-polymer nanocomposite resulted in particles that exhibited significant curling (fig. S8, A and B). The presence of curled particles is detrimental to the quality of coatings, because the curled particles neither pack nor orient themselves in their coatings (fig. S8, C and D). However, the dissolution and purification process reported here was sufficient to obtain flat, crystalline, exfoliated nanosheets capable of producing a highly packed and oriented coating.

The presence of microporosity (fig. S9) within the MWW and MFI layers imparts molecular sieving and hosting capabilities and thus expands the list of available nanosheets amenable to layer-by-layer assembly (*28, 29*) for the fabrication of nanocomposites. Moreover, because of their large lateral area and small thickness, the zeolite nanosheets can coat porous substrates to form well-packed thin deposits. As a result, these nanosheets are attractive materials for the fabrication of thin zeolite membranes. For example, simple filtration of the MFI nanosheet suspension through an anodized alumina membrane (Anopore, pore size 200 nm) followed by calcination for polymer removal resulted in a uniform, well-packed deposit consisting of highly oriented, overlapping, flat nanosheets (Fig. 4A). Even rough porous substrates, such as homemade α-alumina supports with ~200-nm pores, can be coated by filtration to obtain smooth films (Fig. 4, B to D, and E). Figure 4B is a top-view scanning electron microscope (SEM) image of an MFI nanosheet coating on α-alumina, indicating uniform surface coverage. Because the nanosheets are very thin, secondary electrons from the underlying nanosheets can be observed marking their morphology and underscoring the overlap. Cross sections cut by focused ion beam (FIB) were observed by ion-beam microscopy (Fig. 4C) and TEM (Fig. 4, D and E). We observed no penetration of the nanosheets in the interior of the substrate. This is a desirable feature for forming thin zeolite films to achieve high-flux membranes. The nanosheets conform to the substrate surface roughness because of their high aspect ratio and nanometer-range thickness. As a result, neither masking of the support pores (*30*) nor use of smoothened multilayered (asymmetric) membranes (*31*) or functionalization (*32*) is necessary, as in the case of coating from isotropic zeolite nanoparticles or nonisotropic microparticles. However, these films do not show any selectivity for *p-/o*-xylene [a typical mixture that is widely used to assess the molecular sieving

capability of MFI films (*33, 34*)]. It is evident from Fig. 4D and the HRTEM image in Fig. 4E that nanometer-sized gaps exist between the nanosheets. After a single hydrothermal treatment for 4.5 hours at 90°C under conditions that in the absence of nanosheet coating do not result in an observable deposit (molar composition, 60 SiO_2: 9 tetrapropylammonium hydroxide:

8100 H_2O: 240 ethanol; aged at 90°C for 6 hours), the MFI nanosheet film thickness remained unchanged (fig. S10, A to D), whereas the gaps between the nanosheets were reduced, as suggested by the TEM images of the film cross-section (figs. S10, D and E) and an improved separation performance. Five membranes prepared by this method separated xylene isomers
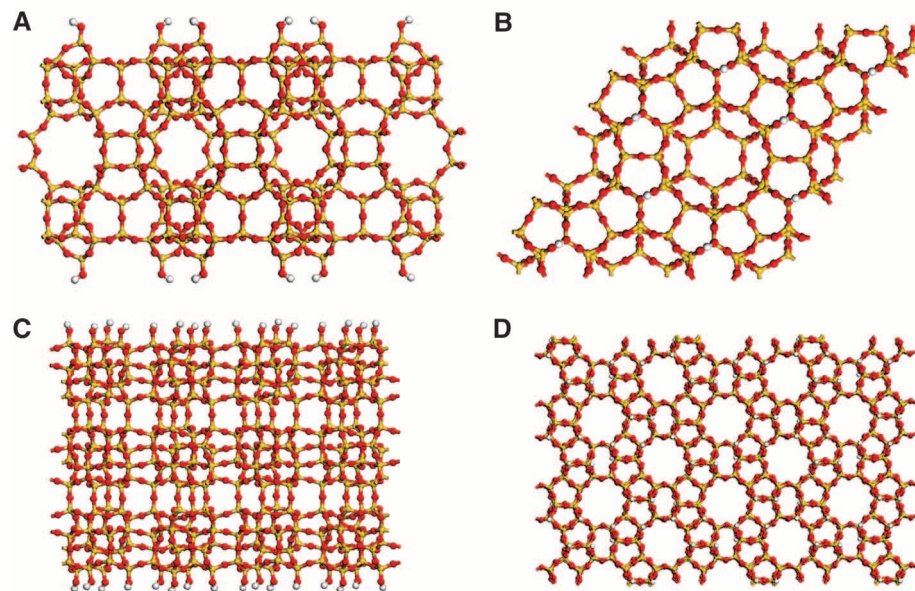

Fig. 3. Relaxed surface structures of the MWW and MFI nanosheets obtained by structure optimization of the 1-unit-cell-thick MWW and 1.5-unit-cell-thick MFI structures with Car-Parrinello molecular dynamics. Si, O, and H atoms are colored in yellow, red, and white, respectively. (**A** and **B**) MWW nanosheet viewed along the *a* (or *b*) axis (A) and along the *c* axis (B). (**C** and **D**) MFI nanosheet viewed along the *c* axis (C) and along the *b* axis (D).

Fig. 4. Images of the MFI nanosheet coating on porous supports. (**A**) SEM image (top view) of the coating of MFI nanosheets on an Anopore disk. The top half of the image shows the bare Anopore support, whereas the bottom half shows a uniform coating of nanosheet on the 200-nm pores of the support. (**B**) SEM image (top view) of the coating of an MFI nanosheet on a homemade porous α-alumina support. (**C**) FIB image of the cross section of the coating in (B). The image was taken by a Ga ion source (30 kV) at a tilt angle of 52°. The nanosheet coating is sandwiched between the FIB-deposited platinum (to protect the coating from milling) and the alumina support. (**D**) TEM image of the cross section of the coating in (B). The dark layer on top of the coating is FIB-deposited platinum. (**E**) HRTEM image of the coating cross section. Scale bars in (A) to (D), 200 nm; in (E), 20 nm.
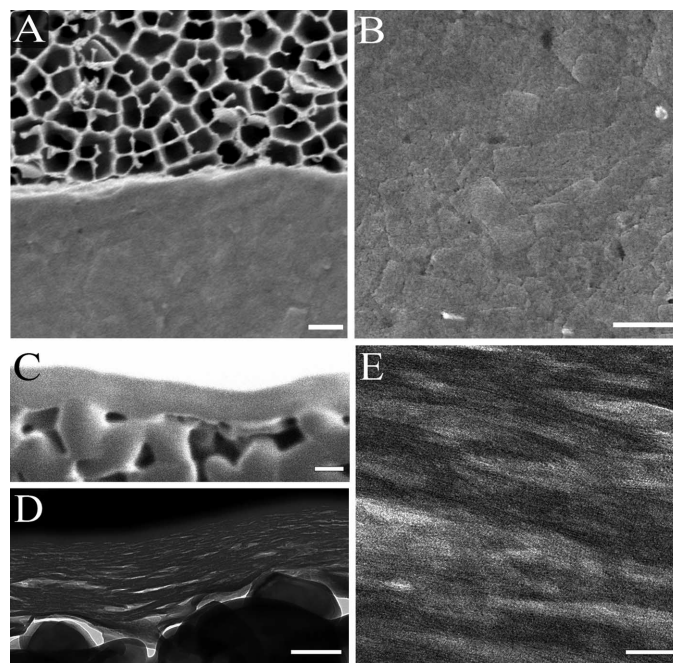
(p-xylene from o-xylene) with a p-xylene/o-xylene separation factor of 40 to 70 and p-xylene permeance of 3×10^{-7} mol m^{-2}s^{-1} Pa^{-1} at 150°C (fig. S11). Preliminary findings from MWW nanosheet coatings show that a seed layer of similar quality to that of MFI nanosheets can be obtained (fig. S12A), which, after secondary growth (fig. S12B), leads to membranes exhibiting molecular sieving properties (fig. S12, C and D) with ideal selectivies for He/H$_2$ and He/N$_2$ up to 3 and 17, respectively, which are different from the values expected from Knudsen diffusion and consistent with the small transport-limited aperture of MWW along the c axis.

These findings indicate that the films fabricated using exfoliated zeolite nanosheets exhibit the expected molecular sieving properties and are appropriate to be used as membranes. The exfoliation and purification process described here may also be applicable to other microporous layered materials to obtain high-aspect-ratio crystalline nanosheets with high purity and uniformity of thickness. Moreover, the simple film formation method introduced, based only on filtration of the nanosheet suspensions, is likely to be easily scalable for large-scale membrane formation on low-cost, commercially available porous supports with large pores and rough surfaces.

References and Notes
1. M. E. Leonowicz, J. A. Lawton, S. L. Lawton, M. K. Rubin, *Science* **264**, 1910 (1994).
2. A. Corma, V. Fornes, S. B. Pergher, T. L. M. Maesen, J. G. Buglass, *Nature* **396**, 353 (1998).
3. M. Choi et al., *Nature* **461**, 246 (2009).
4. M. A. Snyder, M. Tsapatsis, *Angew. Chem. Int. Ed.* **46**, 7560 (2007).
5. M. E. Davis, *Nature* **417**, 813 (2002).
6. C. M. Lew, R. Cai, Y. S. Yan, *Acc. Chem. Res.* **43**, 210 (2010).
7. V. V. Narkhede, H. Gies, *Chem. Mater.* **21**, 4339 (2009).
8. N. Takahashi, H. Hata, K. Kuroda, *Chem. Mater.* **23**, 266 (2011).
9. J. H. Yu, R. R. Xu, *Acc. Chem. Res.* **36**, 481 (2003).
10. Q. M. Gao et al., *J. Solid State Chem.* **129**, 37 (1997).
11. H. M. Yuan et al., *J. Solid State Chem.* **151**, 145 (2000).
12. Z. Li, B. Marler, H. Gies, *Chem. Mater.* **20**, 1896 (2008).
13. G. G. Juttu, R. F. Lobo, *Microporous Mesoporous Mater.* **40**, 9 (2000).
14. I. Ogino et al., *J. Am. Chem. Soc.* **133**, 3288 (2011).
15. L. Liu et al., *Inorg. Chem.* **48**, 4598 (2009).
16. C. Rubio et al., *Eur. J. Inorg. Chem.* **2010**, 159 (2010).
17. W. J. Roth, C. T. Kresge, *Microporous Mesoporous Mater.* **144**, 158 (2011).
18. S. Maheshwari et al., *J. Am. Chem. Soc.* **130**, 1507 (2008).
19. S. Maheshwari, thesis, University of Minnesota, Minneapolis, MN (2009).
20. L. A. Nagahara, K. Hashimoto, A. Fujishima, D. Snowdenlfft, P. B. Price, *J. Vac. Sci. Technol. B* **12**, 1694 (1994).
21. P. Giannozzi et al., *J. Phys. Condens. Matter* **21**, 395502 (2009).
22. See SOM on *Science* Online.
23. J. M. Cowley, A. F. Moodie, *Acta Crystallogr.* **10**, 609 (1957).
24. E. J. Kirkland, R. F. Loane, J. Silcox, *Ultramicroscopy* **23**, 77 (1987).
25. J. L. Schlenker, B. K. Peterson, *J. Appl. Cryst.* **29**, 178 (1996).
26. The UDSKIP algorithm to calculate theoretical powder XRD patterns of ultra-small zeolite crystals is available at www.che.udel.edu/research_groups/nanomodeling/resources.html.
27. P. Wu et al., *J. Phys. Chem. B* **108**, 19126 (2004).
28. S. Srivastava, N. A. Kotov, *Acc. Chem. Res.* **41**, 1831 (2008).
29. M. Osada, T. Sasaki, *J. Mater. Chem.* **19**, 2503 (2009).
30. J. Hedlund, F. Jareman, A. J. Bons, M. Anthonis, *J. Membr. Sci.* **222**, 163 (2003).
31. P. S. Lee et al., *J. Am. Chem. Soc.* **133**, 493 (2011).
32. Z. P. Lai et al., *Science* **300**, 456 (2003).
33. J. Caro, M. Noack, *Microporous Mesoporous Mater.* **115**, 215 (2008).
34. J. Choi et al., *Science* **325**, 590 (2009).

A Major Constituent of Brown Algae for Use in High-Capacity Li-Ion Batteries

Igor Kovalenko,[1] Bogdan Zdyrko,[2] Alexandre Magasinski,[1] Benjamin Hertzberg,[1] Zoran Milicev,[1] Ruslan Burtovyy,[2] Igor Luzinov,[2]* Gleb Yushin[1]*

The identification of similarities in the material requirements for applications of interest and those of living organisms provides opportunities to use renewable natural resources to develop better materials and design better devices. In our work, we harness this strategy to build high-capacity silicon (Si) nanopowder–based lithium (Li)–ion batteries with improved performance characteristics. Si offers more than one order of magnitude higher capacity than graphite, but it exhibits dramatic volume changes during electrochemical alloying and de-alloying with Li, which typically leads to rapid anode degradation. We show that mixing Si nanopowder with alginate, a natural polysaccharide extracted from brown algae, yields a stable battery anode possessing reversible capacity eight times higher than that of the state-of-the-art graphitic anodes.

A typical procedure for the preparation of Li-ion battery electrodes includes mixing electroactive powder with conductive carbon additives and a polymeric binder dissolved in a solvent. The produced slurry is then cast on metal foil current collectors and dried. Traditionally, most research has been focused on synthesis of active powders with improved properties, and less attention was devoted to the advancement of the electrically inactive components of battery electrodes, such as binders. Yet recent studies have shown that many important battery characteristics, including stability and irreversible capacity losses, are critically dependent on the binder's properties (1–4). High-capacity electrochemically active particles that exhibit substantial volume changes during insertion and extraction of Li require improved binder characteristics to ensure electrode integrity during use. Si, in particular, exhibits the largest volume changes during Li-ion battery operation. The interest in Si-based anodes (1, 5–11) stems from the abundance of Si in nature, its low cost, and its high theoretical capacity, which is an order of magnitude higher than that of the conventionally used graphite.

Recent studies have shown that synthetic and bio-derived polymers that contain carboxy groups, such as polyacrylic acid (PAA) and carboxymethyl cellulose (CMC), demonstrate promising characteristics as binders for Si-based anodes (1, 9, 12). Low binder extensibility did not demonstrate a negative effect on the battery performance (12). Reasonably stable anode performance, however, could only be achieved when Si volume changes were minimized by incomplete Li insertion in the tests (9) or accommodated by the use of extra-large binder content (1, 13), which lowers the resulting anode capacity. The polar hydrogen bonds between the carboxy groups of the binder and the SiO$_2$ on the Si surface were proposed to exhibit a self-healing effect and reform if locally broken (1). An alternative explanation for the observed stability of the rigid binders with lower extensibility could be that Si nanoparticles deform plastically during electrochemical alloying with Li (8), expanding toward the existing pores between the particles.

Here, we report that alginate, a high-modulus natural polysaccharide extracted from brown algae, yields a remarkably stable battery anode. Unlike many polysaccharides commonly found

[1]School of Materials Science and Engineering, Georgia Institute of Technology, Atlanta, GA 30332, USA. [2]School of Material Science and Engineering and Center for Optical Materials Science and Engineering Technologies, Clemson University, Clemson, SC 29634, USA.

*To whom correspondence should be addressed. E-mail: luzinov@clemson.edu (I.L.); yushin@gatech.edu (G.Y.)